Joule

Article

Interfacial charge transfer acceleration and thermal stress release for high-performance perovskite/silicon tandem solar cells

Graphical abstract

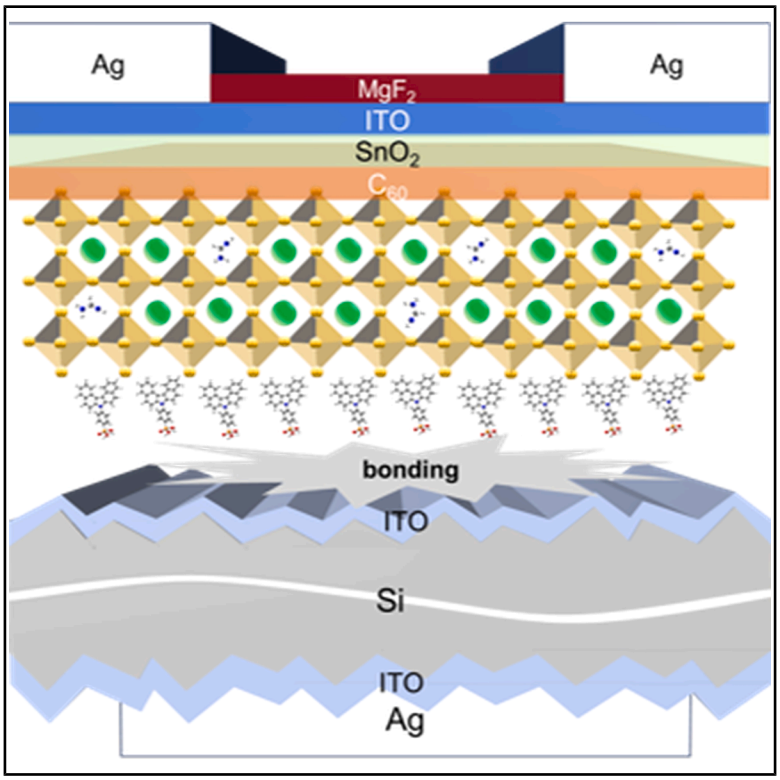

Highlights

- PhPADCB forms uniform SAM contacts on textured silicon
- Rigid molecular anchoring accelerates buried-interface charge transfer
- PhPADCB mitigates thermal stress at the textured buried interface
- Tandem cells reach 33.96% efficiency with robust thermal stability

Authors

Shengjie Du, Mingming Hu, Zhewei Zhang, ..., Enbing Bi, Weijun Ke, Guojia Fang

Correspondence

bienbing@huasunsolar.com (E.B.), weijun.ke@whu.edu.cn (W.K.), gjfang@whu.edu.cn (G.F.)

In brief

Du and colleagues introduce a rigid self-assembled monolayer, PhPADCB, to regulate the textured buried interface in perovskite/silicon tandem solar cells. The molecular design improves conformal contact, accelerates interfacial charge transfer, mitigates thermal stress, and enables efficient and stable tandem photovoltaics.

Du et al., 2027, Joule *11*, 102597
January 20, 2027
https://doi.org/10.1016/j.joule.2026.102597

CellPress

Please cite this article in press as: Du et al., Interfacial charge transfer acceleration and thermal stress release for high-performance perovskite/silicon tandem solar cells, Joule (2026), https://doi.org/10.1016/j.joule.2026.102597

Joule

CellPress

Article

Interfacial charge transfer acceleration and thermal stress release for high-performance perovskite/silicon tandem solar cells

Shengjie Du,[1,5] Mingming Hu,[2,5] Zhewei Zhang,[3,5] Jiwei Liang,[2] Feng Ye,[1] Yangyang Guo,[1] Kaijing Gao,[1] Tie Guo,[3,4] Xiaohua Xu,[3,4] Enbing Bi,[3,4,*] Weijun Ke,[1,*] and Guojia Fang[1,2,6,*]

[1]Key Lab of Artificial Micro- and Nano-Structures of Ministry of Education of China, School of Physics and Technology, Wuhan University, Wuhan 430072, China

[2]School of Electronics and Electrical Engineering, Wuhan Textile University, Wuhan 430200, China

[3]Xuancheng Advanced Solar Technology Institute Co., Ltd., Xuancheng 242000, China

[4]Anhui Huasun Energy Co, Ltd., Xuancheng 242000, China

[5]These authors contributed equally

[6]Lead contact

*Correspondence: bienbing@huasunsolar.com (E.B.), weijun.ke@whu.edu.cn (W.K.), gjfang@whu.edu.cn (G.F.)

https://doi.org/10.1016/j.joule.2026.102597

CONTEXT & SCALE Perovskite/silicon tandem solar cells provide a promising route to exceed the practical efficiency limits of single-junction crystalline silicon photovoltaics. However, translating high-performance wide-band-gap perovskite top cells onto textured silicon substrates remains challenging. The micrometer-scale pyramidal surface complicates uniform self-assembled monolayer formation, weakens buried-interface contact, and aggravates thermal-expansion-mismatch-induced stress during processing and operation. These coupled electrical and mechanical issues can promote nonradiative recombination, ion accumulation, and long-term instability.

This work addresses these challenges by introducing [4-(7H-dibenzo[c]carbazol-7-yl)phenyl]phosphonic acid (PhPADCB), a rigid self-assembled monolayer with strong interfacial anchoring and favorable molecular orientation. The PhPADCB-modified buried interface improves conformal coverage on textured substrates, promotes charge transfer, regulates perovskite crystallization, and mitigates thermally induced interfacial stress. As a result, wide-band-gap perovskite solar cells achieve high efficiency and enhanced operational stability, while perovskite/silicon tandem devices reach an efficiency of 33.96%, with a certified value of 33.72%.

The broader significance of this study is that buried-interface design in tandem photovoltaics should consider not only energy-level alignment and defect passivation but also molecular packing, interfacial anchoring, and mechanical stress accommodation. This molecular regulation strategy provides a practical pathway for developing efficient, stable, and scalable perovskite/silicon tandem solar cells on industry-relevant textured silicon platforms.

SUMMARY

Textured silicon substrates compromise uniform self-assembled monolayer (SAM) formation and aggravate thermal-expansion-mismatch-induced interfacial stress in perovskite/silicon tandem solar cells. Here, we introduce a rigid SAM, [4-(7H-dibenzo[c]carbazol-7-yl)phenyl]phosphonic acid (PhPADCB), to regulate the textured buried interface. Its phenyl-anchored phosphonic acid motif and rigid molecular backbone promote conformal coverage across silicon pyramids, while strong interfacial anchoring stabilizes the buried contact and facilitates interfacial charge transfer. This molecular design reduces defect density and local ion accumulation, improves energy-level alignment, and mitigates tensile stress arising from thermal mismatch. The biphenyl-derived head group further passivates under-coordinated defects, enabling high-quality wide-band-gap perovskite films. Consequently, 1.67 eV devices achieve an efficiency of 23.77% and retain 91% of their initial performance after 1,500 h of maximum power point operation. Perovskite/silicon tandems reach an efficiency of 33.96%, with a certified value of 33.72%, and exhibit robust thermal stability.

Please cite this article in press as: Du et al., Interfacial charge transfer acceleration and thermal stress release for high-performance perovskite/silicon tandem solar cells, Joule (2026), https://doi.org/10.1016/j.joule.2026.102597

INTRODUCTION

Perovskite/silicon tandem solar cells have emerged as one of the most commercially promising photovoltaic technologies.[1–3] By integrating a silicon bottom cell with a perovskite top cell, this architecture exploits the complementary absorption spectra of the two materials, enabling more efficient utilization of the solar spectrum. To date, a certified power conversion efficiency (PCE) of 34.85% has been achieved with this technology.

Textured substrates, while beneficial for light harvesting, complicate the conformal growth of perovskite films and pose challenges for uniform interfacial formation and device scalability.[4] Achieving homogeneous self-assembled monolayers (SAMs) on such topographies remains difficult. Most recently reported monolayered or bilayered SAMs are predominantly constructed from alkyl chain linkers, whose suboptimal symmetry and flexibility often result in non-uniform deposition and molecular stacking.[5,6] This not only compromises hole transport but also promotes defect formation at the perovskite bottom interface.

To address these challenges, recent efforts have focused on developing novel SAMs that improve interfacial compatibility, large-area uniformity, and stability. For example, Li et al. designed 4-(11H-benzo[a]carbazol-11-yl) butylphosphonic acid (4-PhCz), achieving dual-side interfacial reinforcement and enabling a PCE of 22.53% for wide-band-gap perovskite cells and 31.26% for tandem devices.[7] Qin et al. introduced donor-acceptor coplanar conjugated SAMs to address long-standing issues of limited hole transport, instability, and non-uniform deposition, yielding a certified 34.2% efficiency for 1-cm^2 tandems.[2] Additionally, Jen et al. developed a thermally cross-linked co-SAM system that delivered 26.92% efficiency in single-junction devices with exceptional thermal cycling stability.[8] These studies demonstrate that SAM performance is governed not only by head-group chemistry, but also by molecular connectivity, conformational freedom, intermolecular packing, and the collective adaptability of the assembled monolayer.[9]

Previous studies have primarily focused on modifying SAM head groups or employing strategies such as multi-SAMs and cross-linked SAMs while still relying on flexible alkyl chain linkers. Although these approaches offer certain improvements, the inherent flexibility of the linkers can still lead to interfacial molecular aggregation, thereby impeding charge transfer and increasing parasitic resistance. In contrast, we here apply a hole transport material, [4-(7H-dibenzo[c]carbazol-7-yl) phenyl]phosphonic acid (PhPADCB), featuring a phenyl-based conjugated linker and a biphenyl head group, to the challenging context of perovskite/silicon tandems on textured substrates and systematically investigate its underlying interfacial physics. The rigid conjugated backbone effectively suppresses molecular stacking and promotes the formation of a compact monolayer, while the biphenyl head group efficiently passivates defects at the perovskite interface, enhances molecular ordering, and improves crystallinity. Moreover, the strong interfacial binding of PhPADCB to both In_2O_3:Sn (ITO) electrode and the perovskite (100) planes suppresses ionic migration, facilitates energy-level alignment, and reduces interfacial stress accumulation resulting from the thermal-expansion mismatch between the perovskite and silicon, thereby enhancing the thermal stability of tandem devices.

We compared PhPADCB with several conventional SAMs, focusing primarily on [4-(7H-dibenzocarbazol-7-yl)butyl]phosphonic acid (4PADCB). Our results indicate that PhPADCB facilitates interfacial ordering, improves energy-level alignment, and enhances perovskite crystallinity. This modification enables wide-band-gap (1.67 eV) perovskite solar cells to achieve a PCE of 23.77%, retaining 91% of the initial efficiency after 1,500 h of continuous operation. In perovskite/silicon tandem devices, this material delivered a certified PCE of 33.72%. The PhPADCB-modified interface exhibits enhanced structural robustness, with encapsulated tandem cells maintaining 93% of their initial performance after 280 h of thermal cycling (25°C–85°C) and over 90% efficiency after 1,350 h of continuous thermal aging at 65 °C. These findings highlight the potential of rigid molecular interface engineering for developing durable and high-efficiency tandem photovoltaics.

RESULTS AND DISCUSSION

Charge density and MD simulations of PhPADCB

We employed density functional theory (DFT) calculations to model and evaluate the electrostatic potential (ESP) distributions of PhPADCB and four comparator SAM molecules, namely, 2PACz, 4PACz, MeO-2PACz, and 4PADCB. Their calculated dipole moments were 1.97, 2.68, 2.39, 1.55, and 3.21 Debye (D), respectively (Figures 1A and S1). PhPADCB exhibits a dipole moment of 1.97 D, which lies in the moderate range among the investigated SAM molecules. For interfacial SAMs, a dipole moment that is too small often leads to insufficient electronic coupling, whereas an excessively large dipole can cause undesirable band bending and induce interfacial defects. The intermediate dipole of PhPADCB provides a balanced interfacial electric field, and its SAM delivers markedly superior device performance, compared with other SAMs.[10,11]

A recent study comparing PhpPACz, PATPA, and 2PATPA demonstrated that both the conformational characteristics of the head group and the rigidity of the linker critically influence the interfacial electronic and mechanical properties of SAM-based contacts.[9] Although PhpPACz and PhPADCB contain superficially similar aromatic motifs, their molecular configurations are distinctly different. PhpPACz contains a highly constrained carbazole-based head group, whereas the biphenyl-derived terminal moiety of PhPADCB retains a certain degree of rotational freedom around the inter-ring bond. Meanwhile, the conjugated linker of PhPADCB remains structurally rigid, thereby preserving electronic coupling and facilitating interfacial charge transfer. Importantly, the thermal-stress-relaxation capability of the PhPADCB-based SAM should not be attributed to stretching of the individual molecular backbone. Instead, it arises from the collective configurational adaptability of the assembled monolayer through adjustments in molecular orientation, intermolecular spacing, and terminal-group conformation. Therefore, the findings of Yang et al.[9] are complementary to, rather than contradictory with, the present results—appropriate linker rigidity favors efficient electronic coupling, whereas retained conformational freedom within the terminal moiety enables interfacial strain accommodation.

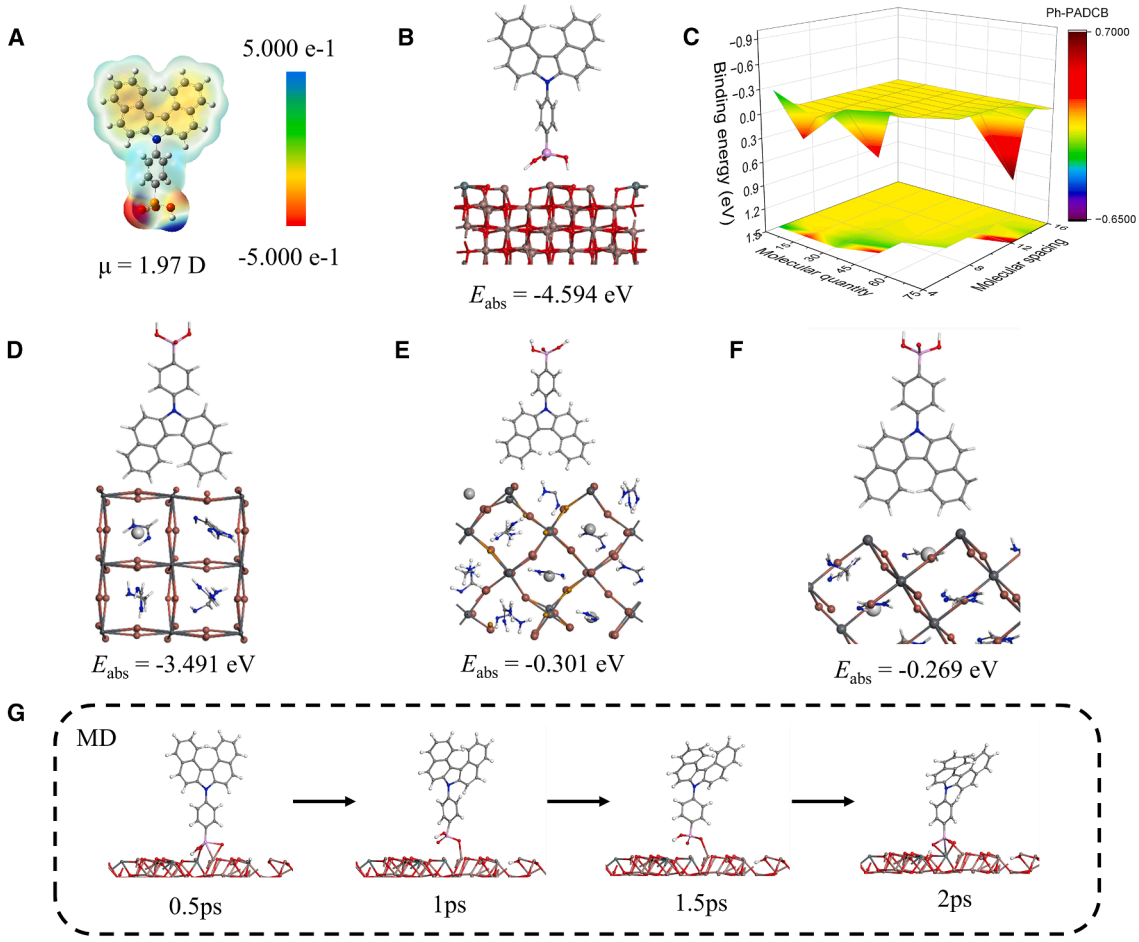

Figure 1. Molecular simulations reveal the strong anchoring, preferred orientation, and facet-selective binding of PhPADCB

(A) ESP of PhPADCB; (B) adsorption energy of the phosphonic acid group of PhPADCB on ITO; (C) schematic illustration of the interaction of PhPADCB as a function of tilt angle and intermolecular spacing; (D–F) adsorption energies of the PhPADCB head group on perovskite (100), (110), and (111) surfaces; (G) MD simulation of PhPADCB relaxation on ITO over time after binding.

The resulting balance between local molecular rigidity and collective monolayer adaptability is closely associated with the favorable molecular orientation and packing order of PhPADCB within the SAM, as further discussed in the following sections.

To theoretically investigate the interfacial interactions between the SAM molecules and the ITO substrate, we calculated their surface binding energies (see Note S1 for computational details). As shown in Figure 1B, the binding energy of PhPADCB on ITO is −4.594 eV, while those of the other SAMs are −2.390 eV for 4PACz, −0.654 eV for MeO-2PACz, and −4.071 eV for 4PADCB (Figure S2). Among these molecules, PhPADCB demonstrates a remarkably strong interfacial affinity toward ITO, indicative of its favorable interfacial anchoring capability.

In addition, we constructed theoretical models to independently examine the intermolecular interactions among identical SAM molecules (see Note S2 for model construction and computational details). The interaction energies were simulated as functions of intermolecular distance and molecular tilt angle (defined as the angle between the molecular axis and the surface normal). The results for PhPADCB are shown in Figure 1C, while those for the other four SAMs are presented in Figure S3. We observed that PhPADCB exhibits stronger intermolecular binding at tilt angles of approximately 0°–15° and 30°–45° (green regions in the projected energy map). Similar behavior is also found for the short-chain SAMs, 2PACz and MeO-2PACz. This indicates that these three molecules tend to adopt a nearly upright orientation relative to the substrate during the self-assembly process. In contrast, 4PADCB and 4PACz, which possess flexible linkers and molecular lengths comparable to that of PhPADCB, show stronger binding at larger tilt angles (45°–60° or 60°–70°). Such a tendency suggests that these molecules are more prone to tilted or stacked configurations when forming SAM layers.[8,12] Importantly, the upright orientation of PhPADCB not only ensures higher-quality and more uniform SAM formation but also enhances interfacial charge transport. The vertical molecular packing provides continuous and efficient electronic pathways, reducing interfacial trap states and facilitating carrier extraction. This dual role of PhPADCB in promoting both SAM uniformity and charge transport contributes directly to the improved device performance.

Please cite this article in press as: Du et al., Interfacial charge transfer acceleration and thermal stress release for high-performance perovskite/silicon tandem solar cells, Joule (2026), https://doi.org/10.1016/j.joule.2026.102597

We further performed theoretical analyses of the interfacial interactions between the SAM molecules and the perovskite crystal during film formation. To this end, different crystallographic surfaces of $FA_{0.73}MA_{0.22}Cs_{0.05}PbI_{2.31}Br_{0.69}$ were cleaved, and the head groups of the SAMs were placed onto these surfaces for adsorption energy simulations (a more negative adsorption energy on a specific surface indicates a higher probability of that facet being exposed during growth, thereby promoting preferential crystal orientation). The adsorption energies of PhPADCB on the (100), (110), and (111) surfaces are shown in Figures 1D–1F, while those of the other four SAM molecules are presented in Figures S4–S6. The simulation results indicate that PhPADCB exhibits the strongest binding to the (100) surface—which is characterized by low defect density, vertical growth relative to the substrate, and optimal charge transport—compared with the other two crystallographic facets, with a binding energy of −3.491 eV. Furthermore, this binding is also the strongest among the five SAM molecules, as the corresponding (100) surface binding energies for the others are −0.961 eV for 2PACz, −0.051 eV for 4PACz, −1.243 eV for MeO-2PACz, and −1.704 eV for 4PADCB. The strong adsorption of PhPADCB on the (100) surface effectively reduces the exposure of other crystallographic facets, thereby promoting the formation of preferential crystal orientation.[13,14]

Subsequently, to further investigate the time-dependent relaxation behavior and structural evolution of SAM molecules on ITO surfaces, molecular dynamics (MD) simulations were performed for individual SAM-ITO systems (details provided in Note S3). The temporal evolution of PhPADCB within 0–2 ps is shown in Figure 1G, while those of the other four SAMs are presented in Figure S7. As can be observed, SAMs with short-linker groups exhibit a stronger ability to remain upright on the ITO surface over time, whereas long-linker SAMs (such as 4PADCB and 4PACz) possess lower rigidity and are more prone to bending during relaxation. Although short-linker SAMs exhibit higher rigidity and smaller bending angles, they tend to lose their interfacial bonding strength with ITO as relaxation proceeds. In contrast, PhPADCB maintains both strong interfacial bonding and overall molecular rigidity, minimizing its deviation from the surface normal. Such characteristics provide the necessary conditions for forming a stable and well-ordered SAM layer.[15] Meanwhile, because the relaxation temperature was set to 600 K to accelerate molecular motion, the results indicate that PhPADCB maintains its anchored configuration under the simulated high-temperature condition.

To enable a more direct comparison, 4PADCB, which has a molecular structure closely resembling that of PhPADCB, was analyzed separately. A representative side-view snapshot (Figure S8) was selected to visualize the extent of molecular folding. It is evident that PhPADCB retains a high degree of rigidity and remains firmly anchored to the ITO surface even after 2 ps, whereas 4PADCB exhibits pronounced bending. The phosphonic acid group of 4PADCB gradually moves away from the ITO surface, leading to weakened and unstable interfacial bonding.[1,12] The detailed mechanism diagram is shown in Figure S9.

This upright configuration is beneficial for several reasons. First, it enables stronger and more well-defined interfacial electronic coupling between the phosphonic acid anchoring group and the ITO surface, which helps establish a favorable interfacial dipole and improves energy-level alignment. Second, the vertical molecular arrangement exposes the functional aromatic groups toward the perovskite side, facilitating more efficient interfacial charge transfer. Third, the ordered and compact SAM packing induced by this configuration contributes to a more uniform interfacial contact and can partially alleviate interfacial mechanical stress during thermal cycling.

Comparison of the binding affinity with ITO

To investigate the surface coverage and uniformity of the four SAM molecules—2PACz, MeO-2PACz, 4PADCB, and PhPADCB—on ITO substrates, we spin-coated these SAMs onto ITO-coated glass and performed X-ray photoelectron spectroscopy (XPS) measurements. Figures 2A and 2B show the XPS spectra of Sn 3d and P 2p, respectively. In our experiments, we found that 4PACz exhibited extremely poor wettability, preventing the perovskite precursor solution from spreading across its surface. Therefore, in the following sections involving perovskite films, 4PACz is excluded from individual analysis. From the comparison of the Sn 3d XPS spectra, it can be observed that the bare ITO exhibits the highest Sn 3d signal intensity, primarily originating from the SnO_X component of ITO.[16,17] As the SAM-related signals on the ITO surface increase, the Sn 3d peak intensity is markedly attenuated and simultaneously shifted toward higher binding energies, indicative of pronounced interfacial electronic interactions. Accordingly, the relative binding strength of the SAMs on ITO can be ranked as PhPADCB > 2PACz > 4PADCB > MeO-2PACz. A similar trend is also observed for the In 3d peaks shown in Figure S10. These experimental observations are in good agreement with the preceding DFT calculations, which predict a stronger interfacial binding of PhPADCB to ITO.

Furthermore, based on the P 2p XPS spectra, the surface coverage of different SAMs on ITO can be quantitatively evaluated using the formula

$$R = \frac{A_P/RSF_P}{A_{Sn}/RSF_{Sn}}, \qquad \text{(Equation 1)}$$

where A_X represents the integrated peak area of element X, and RSF_X denotes the relative sensitivity factor of the corresponding orbital.

The above equation can be further simplified as

$$R_n = R\frac{RSF_{Sn}}{RSF_P} = \frac{A_P}{A_{Sn}}. \qquad \text{(Equation 2)}$$

A larger R_n value indicates higher SAM surface coverage on the ITO surface. The extracted R_n values are summarized in Figure S11, where PhPADCB exhibits the highest R_n of 5.02, representing an approximately 3-fold increase, compared with the other SAMs, and thus a markedly enhanced interaction with the ITO substrate. This result is consistent with the preceding theoretical calculations and can be mainly attributed to its moderate dipole moment together with the uniform ESP distribution imparted by the phenyl-linked group. A similar trend is also observed in the O 1s XPS spectra shown in Figure S12. Meanwhile, the XPS spectra of Pb 4f measured on the bottom surfaces of $FA_{0.73}MA_{0.22}Cs_{0.05}PbI_{2.31}Br_{0.69}$ perovskite films deposited

Please cite this article in press as: Du et al., Interfacial charge transfer acceleration and thermal stress release for high-performance perovskite/silicon tandem solar cells, Joule (2026), https://doi.org/10.1016/j.joule.2026.102597

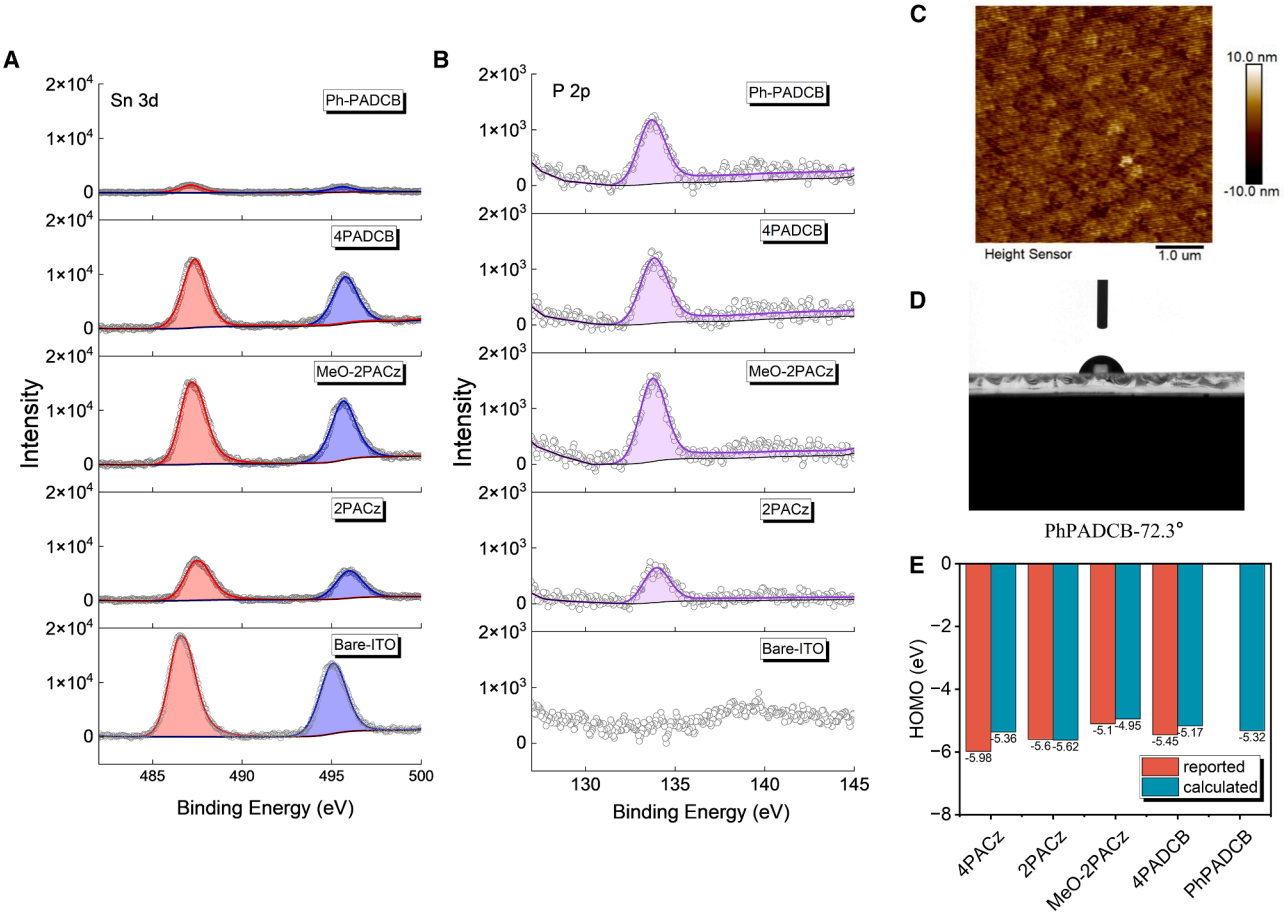

Figure 2. PhPADCB forms a uniform and strongly anchored SAM on ITO

(A) XPS spectra of the Sn 3d peaks for four SAM-modified ITO substrates and pristine ITO; (B) P 2p peaks; (C) AFM image of the PhPADCB surface; (D) water contact angle measurement of the PhPADCB surface; and (E) theoretically calculated and literature-reported HOMO energy levels of the five SAMs.

onto the four different SAM layers are shown in Figure S13. The Pb 4f peaks of 2PACz, MeO-2PACz, 4PADCB, and PhPADCB shift progressively toward lower binding energies, which can be primarily attributed to a reduction in the interfacial Pb potential barrier. Strong interfacial binding typically implies closer and more uniform contact between the SAM molecules and the perovskite surface. After spin-coating, PhPADCB molecules anchor to ITO through the phosphonic acid groups, forming a relatively uniform molecular coverage. This coverage partially attenuates the signals from the underlying ITO while introducing characteristic signals from the molecular components, leading to the observed variations in peak areas. In addition, the strong anchoring interaction between PhPADCB and ITO can slightly modify the local electronic environment at the interface.[3,8,18]

The intrinsic properties of the SAMs on ITO were investigated through atomic force microscopy (AFM) scans (Figure 2C) and water contact angle measurements (Figure 2D). Compared with the other SAM layers (Figure S14), PhPADCB exhibited the lowest root-mean-square (RMS) roughness (RMS = 1.91 nm), further confirming its uniform and smooth coverage.[19] In the water contact angle tests (Figure S15), 4PACz displayed the largest value of 80.1°, which correlates with the poor wetting of perovskite precursor solution on its surface. By contrast, PhPADCB exhibited a moderate contact angle of 72.3°, slightly higher than those of 4PADCB and 2PACz, whereas MeO-2PACz showed stronger hydrophilicity due to its surface methoxy groups (SAMs with short-linker groups, such as 2PACz and MeO-2PACz, tend to form less compact and ordered monolayers compared with those with longer linkers, resulting in smaller water contact angles).[20,21] The phenyl head groups of the SAMs are intrinsically hydrophobic; therefore, a larger water contact angle reflects a denser and more uniform molecular arrangement.[22,23] At the same time, the PhPADCB layer maintains good wetting for the perovskite precursor, achieving a balance between wettability and SAM uniformity.

Furthermore, we performed ultraviolet photoelectron spectroscopy (UPS) measurements on the bottom interface of perovskite films deposited onto glass, with the corrected Fermi edge and secondary electron cutoff determined to be 0.52 and 16.30 eV, respectively (Figure S16). Combining these results with the highest occupied molecular orbital (HOMO) energy levels of the five SAMs, as obtained from DFT calculations (Figure 2E), we

Please cite this article in press as: Du et al., Interfacial charge transfer acceleration and thermal stress release for high-performance perovskite/silicon tandem solar cells, Joule (2026), https://doi.org/10.1016/j.joule.2026.102597

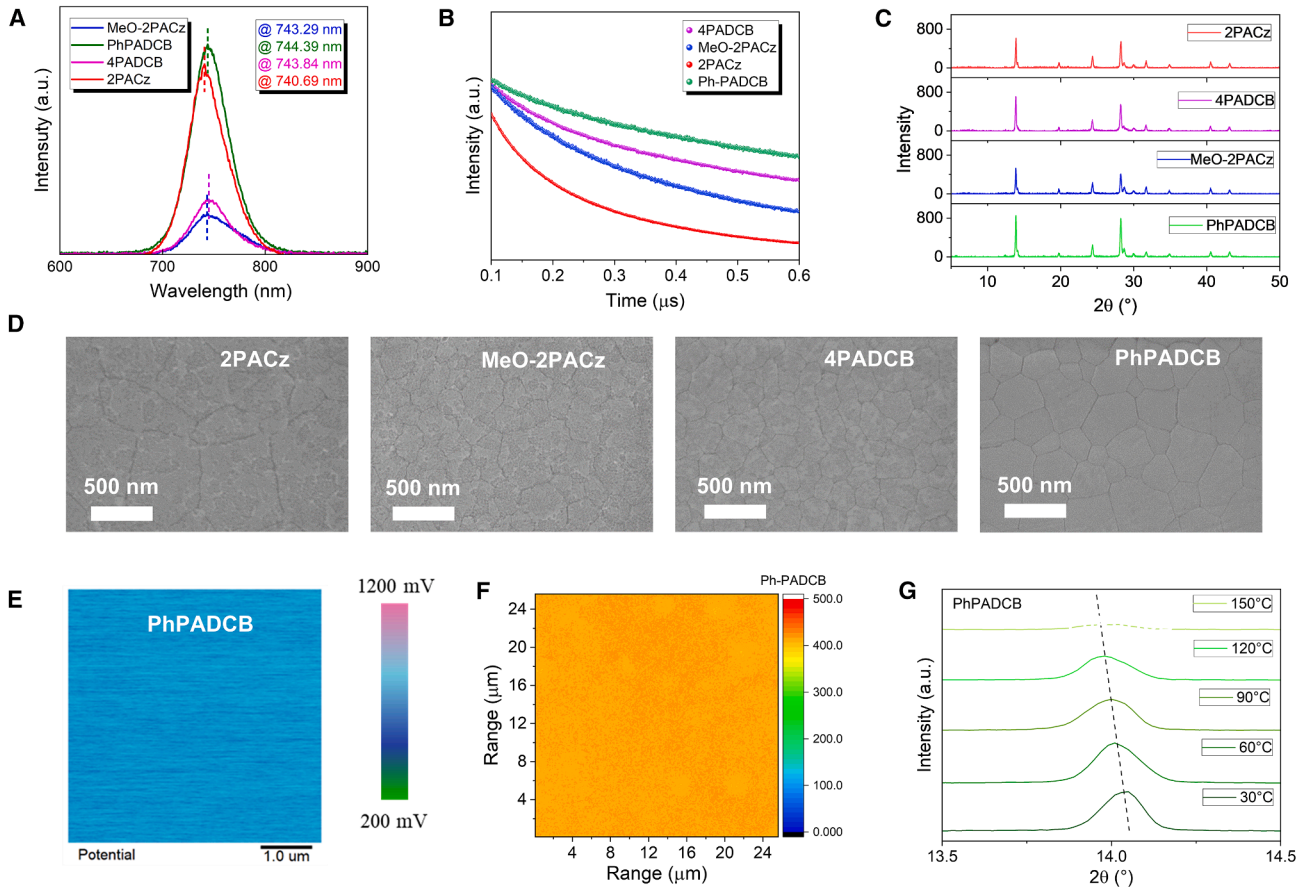

Figure 3. PhPADCB improves wide-band-gap perovskite film uniformity, crystallinity, and buried-interface thermal stability

(A) Steady-state PL spectra of perovskite films deposited on four different SAM-modified substrates; (B) TRPL decay curves of the corresponding films; (C) XRD patterns of perovskite films deposited on different SAM layers; (D) SEM images of perovskite films grown on four SAM layers; (E) KPFM images of perovskite films grown on PhPADCB; (F) PL mapping image of the perovskite film prepared on PhPADCB; (G) XRD peak-position profiles of PhPADCB-based perovskite bottom interfaces after annealing at different temperatures for 10 min.

constructed the energy-level alignment at the perovskite/SAM interface (Figure S17). The valence band maximum (VBM) of the perovskite at the bottom interface was found to be −5.44 eV—showing the closest alignment with PhPADCB, 4PADCB, and 4PACz—whereas larger offsets were observed for MeO-2PACz and 2PACz, potentially leading to electron leakage or impeded hole transport.[24,25] For reference, Figure 2E also presents previously reported experimental values, which exhibit minor deviations from the theoretical predictions.[24,26–28]

Analysis of perovskite film uniformity and optoelectronic and thermal characteristics on different SAMs

The impact of different SAMs on the performance of perovskite will be presented in sequence. Steady-state photoluminescence (PL) and time-resolved PL (TRPL) spectra of perovskite films deposited onto the four SAM-modified substrates (due to wetting issues, 4PACz was excluded from further investigation) are shown in Figures 3A and 3B.

The PL peak positions for MeO-2PACz, 4PADCB, and PhPADCB all appear around 744 nm, corresponding to a band gap of approximately 1.67 eV. In contrast, 2PACz exhibits a slightly blueshifted peak at 740 nm, compared with the other three SAMs, which may arise from differences in film composition or crystallization induced by the underlying SAM. Notably, the perovskite films grown on the PhPADCB-based SAM layer display a stronger PL intensity, indicative of improved crystallinity. Figure 3B shows the TRPL decay of perovskite films on different SAM layers, which were fitted using a bi-exponential function according to Equation 3.

$$I(t) = A_1 e^{-\frac{t}{\tau_1}} + A_2 e^{-\frac{t}{\tau_2}}. \quad \text{(Equation 3)}$$

Here, I(t) corresponds to the fluorescence intensity at time t; τ_1 and τ_2 represent the carrier lifetimes associated with surface defect recombination and bulk radiative recombination, respectively; and A_1 and A_2 correspond to the amplitudes of the respective exponential components. The curves were fitted using a bi-exponential function, and the fitting results are summarized in Table S1. A larger τ_1 indicates that trap-assisted and nonradiative recombination at the interface are partially suppressed, while a larger τ_2 reflects improved bulk crystallinity and reduced nonradiative losses. The perovskite film based on PhPADCB

Please cite this article in press as: Du et al., Interfacial charge transfer acceleration and thermal stress release for high-performance perovskite/silicon tandem solar cells, Joule (2026), https://doi.org/10.1016/j.joule.2026.102597

exhibits the highest τ_1 (82.14 ns) and τ_2 (587.06 ns) values among the four SAM-modified samples. We calculated the carrier average lifetime using the following quadratically weighted formula:

$$\tau_{avg} = \frac{A_1\tau_1^2+A_2\tau_2^2}{A_1\tau_1+A_2\tau_2}, \quad \text{(Equation 4)}$$

where A_1 and A_2 are the exponential amplitudes, and τ_1 and τ_2 are the corresponding carrier lifetimes associated with the fast and slow decay processes, respectively.

Considering the amplitudes A_1 and A_2, the calculated amplitude-weighted average lifetime of PhPADCB reaches 557.96 ns, further demonstrating its pronounced advantage. Therefore, perovskite films deposited onto the PhPADCB layer exhibit superior crystallinity and reduced carrier recombination at the interface, compared with those on other SAMs.[29–31] Furthermore, we selected 4PADCB, a representative SAM with an alkyl linker, and PhPADCB, and we spin-coated perovskite films atop each. PL was measured from the glass side to evaluate the hole-extraction capability of the SAMs. As shown in Figure S18, the PL peak of PhPADCB is lower than that of 4PADCB, indicating more efficient hole extraction.

We performed X-ray diffraction (XRD) measurements on the perovskite films deposited onto the four SAM layers, as shown in Figure 3C. All $FA_{0.73}MA_{0.22}Cs_{0.05}PbI_{2.31}Br_{0.69}$ films exhibit a preferential (100) orientation on the four SAMs. The corresponding full width at half maximum (FWHM) values are presented in Figure S19A, with the perovskite on PhPADCB showing the smallest FWHM of 0.16.

Comparing the XRD peak intensities among the four SAMs, we found that the (110) peak near 24° exhibits approximately equal intensity and is thus used as a reference. The ratio of the (100) to (110) peak intensities for perovskites on the four SAMs is shown in Figure S19B, with PhPADCB exhibiting the highest ratio of 3.62. This is consistent with the previous theoretical calculations, which indicated stronger binding of PhPADCB to the (100) plane, leading to increased exposure of this plane and enhanced preferential orientation.[32,33]

Meanwhile, we performed grazing-incidence wide-angle X-ray scattering (GIWAXS) measurements on the four perovskite films to assess the influence of different SAMs on crystal orientation, as shown in Figure S20. The diffraction rings of the perovskite films on the four SAMs show no significant differences in intensity along the q_x direction. However, along the q_z direction, the perovskite on PhPADCB exhibits a higher intensity compared with the others. The enhanced intensity along the q_z direction implies an increased population of the (100) planes, indicating a more favorable (100) crystallographic orientation, compared with perovskite films grown on the other SAMs. This observation is consistent with the XRD results.[34,35] The (100) planes of the perovskite exhibit superior charge transport efficiency and tend to grow more vertically relative to the substrate. However, they are also prone to enhanced ionic migration. The strong interaction between PhPADCB and the underlying (100) planes helps to stabilize surface coordination, thereby suppressing the escape of ions such as I^- and MA^+ from the lattice and, consequently, mitigating interfacial degradation and phase segregation at their source.

To directly investigate the interaction at the SAM-perovskite bottom interface, perovskite films were deposited onto the four SAMs, followed by curing with AB glue and subsequent delamination of the bottom interface. Examination of the bottom surfaces of these perovskite films by scanning electron microscopy (SEM) yields the following observations (Figure 3D).

For 2PACz, the bottom-interface grains exhibit large variability, with diameters ranging from ~100 to nearly 500 nm, indicating local inhomogeneity of the perovskite, consistent with the limited uniform coverage of the short-chain 2PACz. For MeO-2PACz, the grains are relatively small (~100–150 nm); moreover, due to the weak interaction between MeO-2PACz and ITO (Figure S2), partial delamination occurs during peeling, resulting in a rougher SEM appearance. For 4PADCB, the grains are also small, likely due to uneven distribution and the formation of localized strong adsorption sites that increase nucleation density. In contrast, the perovskite on PhPADCB exhibits a smooth bottom interface with uniformly sized grains, indicating homogeneous nucleation and a more evenly distributed surface energy at the interface.[36,37] PhPADCB not only anchors strongly to ITO but also interacts favorably with the perovskite without damaging its crystal structure.

Meanwhile, cross-sectional images of the four perovskite films are shown in Figure S21, with all films exhibiting a thickness of approximately 500 nm. The perovskite on PhPADCB shows reduced grain stacking, a more vertical orientation relative to the substrate, and fewer gaps at the bottom interface.

To further investigate the energy-level alignment, perovskite films were deposited onto four different SAMs and characterized using Kelvin probe force microscopy (KPFM), as shown in Figures 3E and S22. The obtained images represent the contact potential difference (CPD) between the probe and the bottom surface of perovskite films. After calibration using the work function of graphene (4.4 eV), the corresponding work functions (W_F) of perovskite films grown on different SAMs were determined to be 5.06 eV for PhPADCB, 5.09 eV for 2PACz, 4.66 eV for MeO-2PACz, and 4.75 eV for 4PADCB. The detailed CPD distribution is shown in Figure S23.

As shown in Figure S17, the Fermi level of the bottom interface of perovskite grown without a SAM is −4.92 eV, while its HOMO level is −5.44 eV. Different SAMs exert a direct influence on the energy-level alignment of the perovskite. PhPADCB and 2PACz slightly lower the Fermi level of the underlying perovskite, whereas MeO-2PACz and 4PADCB elevate it. Notably, the HOMO level of 2PACz is −5.62 eV, exhibiting a significant mismatch with the perovskite HOMO at the bottom interface, which may hinder hole transport. By contrast, PhPADCB achieves a more favorable energy-level alignment with the perovskite. The surface potential roughness of the four perovskite bottom interfaces is also shown in Figure S22, among which the PhPADCB-based film exhibits an RMS of 14.8 mV, indicating a relatively smoother potential distribution.[38]

To further elucidate the influence of the four SAMs on the uniformity of the perovskite films, we conducted PL mapping measurements on perovskite layers deposited atop each SAM, as shown in Figures 3F and S24. The results reveal that the perovskite films formed on PhPADCB and 2PACz exhibit markedly higher PL uniformity than those on 4PADCB and MeO-2PACz. Moreover, the overall PL intensity of the perovskite on PhPADCB is superior to

Please cite this article in press as: Du et al., Interfacial charge transfer acceleration and thermal stress release for high-performance perovskite/silicon tandem solar cells, Joule (2026), https://doi.org/10.1016/j.joule.2026.102597

that on 2PACz. Taken together, these findings demonstrate that the perovskite fabricated on PhPADCB possesses the most favorable luminescent performance and crystalline quality among the four SAM-based perovskite films.[39]

Building on our earlier results, we determined that 4PADCB and PhPADCB offer superior overall interfacial performance, compared with the other SAMs. Consequently, we conducted a dedicated evaluation of the thermal stability at the buried perovskite interfaces formed on these two SAMs. Perovskite films grown on the experimentally prepared SAMs were annealed in air at 30°C, 60°C, 90°C, 120°C, and 150°C for 10 min, after which XRD measurements were performed. The evolution of the diffraction features under these thermal conditions is summarized in Figures 3G, S25, and S26, which collectively provide a clear comparison of the stability differences between the two interfaces. For both samples, the perovskite diffraction peaks decrease in intensity with increasing annealing temperature. Focusing on the (100) reflection as the primary indicator, the peak progressively shifts toward lower angles as the temperature rises, corresponding to an increased lattice spacing and thus tensile strain. Notably, the perovskite grown on PhPADCB exhibits substantially lower tensile strain than that on 4PADCB.

Furthermore, to investigate the depth-dependent effects of thermal annealing on the buried interfaces of the two perovskite films, we annealed both samples in air at 120°C for 30 min. After cooling, the perovskite films were once again peeled off from the glass substrates, and depth-dependent GIXRD measurements were performed on the buried interfaces. The results are shown in Figures S27 and S28. The data reveal that following thermal annealing and cooling, the buried interface of the perovskite film grown on PhPADCB exhibits a smaller tensile strain. In contrast, the perovskite on 4PADCB shows a larger tensile strain at the buried interface, which is primarily concentrated in the near-surface region, indicating a more severe disruption of the crystal lattice.

The XRD experiments conducted on the buried perovskite interface demonstrate that PhPADCB enhances its thermal stability.

Performance analysis of perovskite devices fabricated on 4PADCB and PhPADCB

We fabricated perovskite solar cells based on four different SAMs and compiled statistical plots of the PCE, fill factor (FF), and open-circuit voltage (V_{OC}), as shown in Figure S29. The devices ranked by PCE from highest to lowest correspond to SAM layers of PhPADCB, 4PADCB, MeO-2PACz, and 2PACz, with the same trend observed for the $V_{OC} \times$ FF statistics. We selected the two highest-efficiency SAMs for further device performance comparison to directly illustrate the enhancement imparted by PhPADCB. The single-junction device architecture is shown in Figure 4A, consisting of glass/ITO/SAM/$FA_{0.73}MA_{0.22}Cs_{0.05}PbI_{2.31}Br_{0.69}$/$C_{60}$/BCP/Cu.

The *J-V* curves of the best-performing single-junction devices based on 4PADCB and PhPADCB are presented in Figure 4B. The device based on PhPADCB exhibits a maximum reverse-scan PCE of 23.77%, with a V_{OC} of 1.27 V, an FF of 84.63%, and a short-circuit current density (J_{SC}) of 22.13 mA/cm^2. In comparison, the best 4PADCB device shows a reverse-scan PCE of 22.87%, a V_{OC} of 1.26 V, an FF of 82.73%, and a J_{SC} of 21.94 mA/cm^2. The performance improvement is mainly reflected in the J_{SC} and FF, likely arising from enhanced charge transport, improved film uniformity, and interfacial passivation. The *J-V* curves of the best-performing perovskite devices fabricated with 2PACz and MeO-2PACz are shown in Figure S30, and the photovoltaic parameters of the best devices based on the four SAMs are summarized in Table S2.

To further understand the carrier recombination dynamics in the devices, the dependence of the J_{SC} and V_{OC} on the incident light intensity (P) was investigated. The J_{SC}follows a power-law relationship with P, expressed as formula

$$J_{SC} \propto P^{\alpha}, \qquad \text{(Equation 5)}$$

where the exponent α reflects the degree of bimolecular recombination within the device. An α value close to unity indicates efficient charge extraction and negligible bimolecular recombination losses. The α value of the PhPADCB-based device is 0.978, higher than that of the 4PADCB-based device (0.936), suggesting that the PhPADCB-modified interface facilitates more efficient carrier transport and suppresses nonradiative recombination losses (Figure 4C).[40]

Furthermore, the dependence of V_{OC} on light intensity follows the formula

$$V_{OC} = \frac{nkT}{q} \ln (P) + C, \qquad \text{(Equation 6)}$$

where n is the ideality factor, k is the Boltzmann constant, T is the absolute temperature, q is the elementary charge, and C is a constant related to the dark saturation current. The ideality factor n provides insights into the recombination mechanism—values approaching 1 indicate radiative (band-to-band) recombination, while values exceeding 1 imply trap-assisted (Shockley-Read-Hall) recombination. The PhPADCB-based device exhibits a smaller slope (n = 1.19) in the V_{OC}-ln (P) plot, compared with the 4PADCB-based device (n = 1.54), indicating reduced trap-mediated recombination and lower nonradiative losses, consistent with its enhanced photovoltage and overall device performance (Figure S31). Subsequently, the steady-state power output (SPO) was evaluated for both devices. As shown in Figure 4D, after 600 s of continuous operation, the PhPADCB-based device maintained a stable PCE of 23.43%, whereas the 4PADCB-based device retained 22.59%. This result confirms the superior operational stability and sustained power delivery of the PhPADCB-modified perovskite interface, compared with those of 4PADCB.

Subsequently, capacitance-voltage (*C-V*) measurements were performed on both devices to further elucidate their built-in potential and defect characteristics. The *C-V* data were analyzed using the Mott-Schottky relation

$$C^{-2} = \frac{2(V_{bi} - V)}{q\varepsilon N}, \qquad \text{(Equation 7)}$$

where C is the device capacitance, q is the elementary charge, ε is the dielectric permittivity, N is the apparent carrier concentration, V_{bi} is the built-in potential, and V is the applied bias. The depletion width W_d was further determined using

$$W_d = \sqrt{\frac{2\varepsilon(V_{bi} - V)}{qN}}. \qquad \text{(Equation 8)}$$

Please cite this article in press as: Du et al., Interfacial charge transfer acceleration and thermal stress release for high-performance perovskite/silicon tandem solar cells, Joule (2026), https://doi.org/10.1016/j.joule.2026.102597

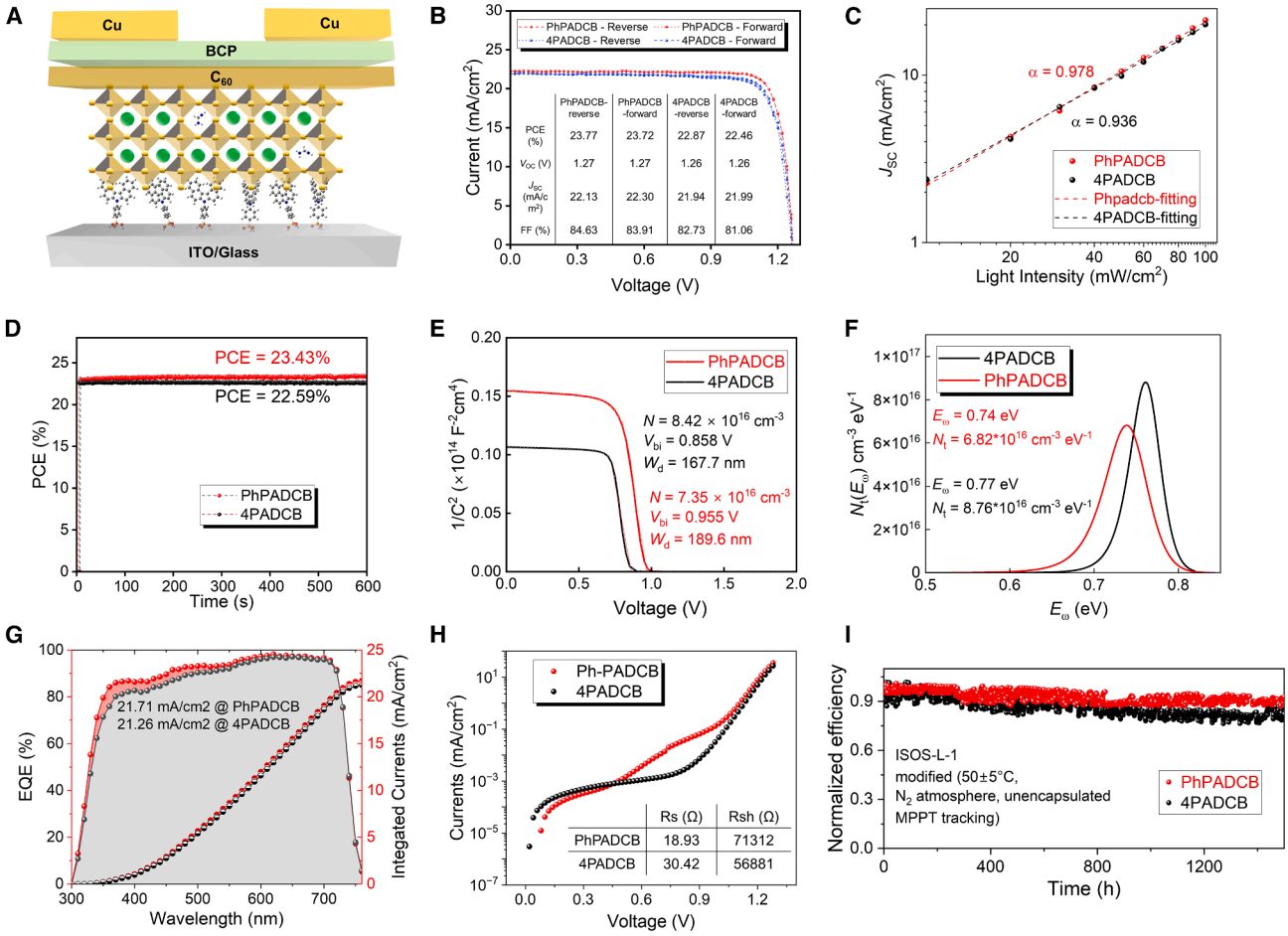

Figure 4. PhPADCB enhances charge extraction, suppresses recombination, and improves operational stability in wide-band-gap perovskite solar cells

(A) Schematic illustration of the single-junction perovskite solar cell architecture; (B) best *J-V* curves and corresponding parameters of perovskite devices based on 4PADCB and PhPADCB SAMs; (C) short-circuit current as a function of light intensity for the two devices; (D) maximum SPO of the two devices; (E) *C-V* curves; (F) t-DOS plots of the two devices; (G) EQE; (H) dark *J-V* curves; (I) MPPT outputs of the two devices.

The fitted curves are shown in Figure 4E. The extracted parameters indicate that the 4PADCB-based device exhibits a V_{bi} of 0.858 V, a W_d of 167.7 nm, and a defect density N of 8.42×10^{16} cm^{-3}. In contrast, the PhPADCB-based device shows a higher V_{bi} of 0.955 V, a larger W_d of 189.6 nm, and a lower N of 7.35×10^{16} cm^{-3}.[41]

These results clearly indicate that the PhPADCB-based device exhibits a higher built-in potential, a lower carrier trap density, and an increased W_d, which contribute to driving photogenerated carrier separation and transport, reducing bulk defects, and enhancing charge separation efficiency, respectively.

The electrochemical impedance spectroscopy (EIS) of the two perovskite devices was further measured, as shown in Figure S32. The resulting Nyquist plots display two semicircles, where the low-frequency semicircle is typically associated with charge accumulation and ion migration, while the high-frequency semicircle corresponds to interfacial charge transport. The EIS data were fitted using the following relation:

$$Z(\omega) = R_s + \frac{R_{tr}}{1+j\omega R_{tr}C_{tr}} + \frac{R_{rec}}{1+j\omega R_{rec}C_{rec}}. \quad \text{(Equation 9)}$$

From the fitting, the PhPADCB-based device exhibits $R_{tr} = 0.98$ kΩ and R_{rec} = 2.56 kΩ, whereas the 4PADCB-based device shows R_{tr} = 1.21 kΩ and R_{rec} = 1.86 kΩ. These results indicate that the PhPADCB device has a higher recombination resistance and lower transport resistance, corresponding to reduced interfacial recombination and improved interfacial charge transport.[42]

The space-charge-limited current (SCLC) measurements of devices containing only the hole transport layer (Figure S33) were fitted using

$$J = qn_0\mu\frac{V}{L}, \quad \text{(Equation 10)}$$

where J is the current density, q is the elementary charge, n_o is the intrinsic carrier concentration, μ is the carrier mobility, V is the applied voltage, and L is the device thickness.

Please cite this article in press as: Du et al., Interfacial charge transfer acceleration and thermal stress release for high-performance perovskite/silicon tandem solar cells, Joule (2026), https://doi.org/10.1016/j.joule.2026.102597

As the voltage increases and the traps are filled, the current exhibits a quadratic dependence on voltage:

$$J = \frac{9}{8}\varepsilon_0\varepsilon_r\mu\frac{V^2}{L^3}, \quad \text{(Equation 11)}$$

where ε_0 is the vacuum permittivity, and ε_r is the relative permittivity of the material. By fitting the SCLC data, the trap-filled limit voltages (V_{TFL}) for devices based on 4PADCB and PhPADCB were determined to be 0.44 and 0.31 V, respectively, corresponding to trap densities (N_t) of 4.93×10^{15} and 2.55×10^{15} cm^{-3}. The lower V_{TFL} and N_t values for PhPADCB indicate fewer defects and superior perovskite quality.

As shown in Figure 4F, the density of states (DOS) distribution as a function of the energetic position E_ω was derived from thermal admittance spectroscopy (TAS) measurements conducted at room temperature (300 K). The DOS was calculated from the frequency-dependent capacitance $C(\omega, T)$ according to the following relationship:

$$N_t(E_\omega) = -\frac{V_{bi}}{qkTW_D}\frac{dC}{d\ln(\omega)}, \quad \text{(Equation 12)}$$

where $N_t(E_\omega)$ denotes the trap DOS at the thermal activation energy E_ω, V_{bi} is the built-in potential, q is the elementary charge, and W_D represents the depletion width. The energetic position E_ω corresponding to each frequency was obtained using the temperature-dependent emission rate model:

$$E_\omega = kT\ln\left(\frac{2\beta N_c}{\omega}\right), \quad \text{(Equation 13)}$$

where k is the Boltzmann constant, T is the absolute temperature, N_C is the effective DOS in the conduction band, $\omega = 2\pi f$ is the angular frequency, and β is the carrier capture coefficient.

Due to the influence of interfacial charge accumulation and signal noise, the high-frequency region (corresponding to low E_ω) associated with shallow trap states was excluded from the analysis. Instead, we focus on the low-frequency region (high E_ω), which reflects the deep-trap states within the perovskite absorber. As shown in Figure 4F, the 4PADCB-based device exhibits a distinct deep-trap feature at $E_\omega = 0.77$ eV, corresponding to a trap density of 8.76×10^{16} $cm^{-3}eV^{-1}$. In contrast, the PhPADCB-based device shows a shallower trap feature at $E_\omega = 0.74$ eV with a lower trap density of 6.82×10^{16} $cm^{-3}eV^{-1}$. These results indicate that the PhPADCB-based device contains fewer deep-level traps and that the corresponding trap states lie at lower energetic positions, which are less detrimental to nonradiative recombination processes.

Furthermore, the DOS spectra measured at different temperatures (250–320 K, Figures S34 and S35) show consistent trends with those obtained at room temperature, confirming the robustness of these observations. This further substantiates that the incorporation of PhPADCB effectively reduces deep-level defects and improves the defect landscape of the perovskite absorber.

The external quantum efficiency (EQE) spectra of the two SAM-based devices are shown in Figure 4G. The integrated current density of the PhPADCB-based device reaches 21.71 mA cm^{-2}, which is higher than that of the 4PADCB-based device (21.26 mA cm^{-2}). A pronounced enhancement is observed in the 300- to 500-nm wavelength region and a moderate increase appears in the 500- to 700-nm region, which can be attributed to the interfacial position of PhPADCB at the bottom contact. In addition, the overall improvement in EQE benefits from the enhanced perovskite film quality induced by PhPADCB.

By fitting the dark J-V curves shown in Figure 4H, the series and shunt resistances of the 4PADCB- and PhPADCB-based devices were extracted. The PhPADCB-based device exhibits a series resistance of 18.93 Ω, which is lower than that of the 4PADCB-based device (30.42 Ω), and a shunt resistance of 71,312 Ω, which is higher than that of 4PADCB (59,881 Ω). These results indicate that the PhPADCB-based device possesses superior charge transport properties and reduced leakage pathways, leading to enhanced overall device performance.

Finally, under the ISOS-L-1 standard, the maximum power point tracking (MPPT) stability of the unencapsulated devices was evaluated inside a nitrogen-filled glovebox, as shown in Figure 4I (the actual operating temperature is approximately 50°C). After 1,500 h of continuous illumination, the PhPADCB-based device retained 91% of its initial PCE, whereas the 4PADCB-based device maintained only 85%. This clearly demonstrates that the incorporation of PhPADCB significantly enhances the operational stability of the perovskite devices.

Perovskite/silicon tandem solar cells were subsequently fabricated, with the detailed device architecture illustrated in Figure 5A, comprising an Ag-bottom electrode/ITO/Si-subcell/ITO/SAM/perovskite/C_{60}/SnO_2/ITO/Ag-top electrode/MgF_2 (the cross-sectional image of the perovskite prepared on the silicon surface is shown in Figure 5B, where the perovskite layer has a thickness of approximately 1 μm). The highest-performing devices employing PhPADCB and 4PADCB are shown in Figure 5C; the PhPADCB-based tandem device exhibits a PCE of 33.96%, with a V_{OC} of 1.95 V, a J_{SC} of 20.48 mA/cm^2, and an FF of 85.10%. In comparison, the 4PADCB-based tandem device delivers a PCE of 31.45%, with a V_{OC} of 1.94 V, a J_{SC} of 19.70 mA/cm^2, and an FF of 82.50% (the detailed certification report is shown in Figures S36–S40). The structure of the silicon bottom cell and the cross-sectional SEM image of the 4PADCB-based tandem device are shown in Figure S41. The statistical distribution of device efficiencies is shown in Figure 5D, revealing that PhPADCB-based devices exhibit an average efficiency approximately 2 percentage points higher than those based on 4PADCB. The FF distribution, presented in Figure S42A, further shows that PhPADCB devices achieve an average FF that is 3 percentage points higher than that of their 4PADCB counterparts. Meanwhile, the comparison of V_{OC} and J_{SC} for the two devices is shown in Figures S42B and S42C, with the parameters of the best-performing devices based on the two SAMs summarized in Table S3. The EQE of the best tandem devices based on PhPADCB and 4PADCB is shown in Figure 5E. For the PhPADCB-based device, the currents of the perovskite and silicon sub-cells are 20.35 and 20.19 mA/cm^2, respectively, whereas those for the 4PADCB-based device are 20.03 and 20.16 mA/cm^2. In addition, the SPO of the tandem cell is presented in Figure 5F. After 600 s of illumination, the efficiency of the PhPADCB device reaches 33.45%, while that of the 4PADCB device is 31.89%.

Please cite this article in press as: Du et al., Interfacial charge transfer acceleration and thermal stress release for high-performance perovskite/silicon tandem solar cells, Joule (2026), https://doi.org/10.1016/j.joule.2026.102597

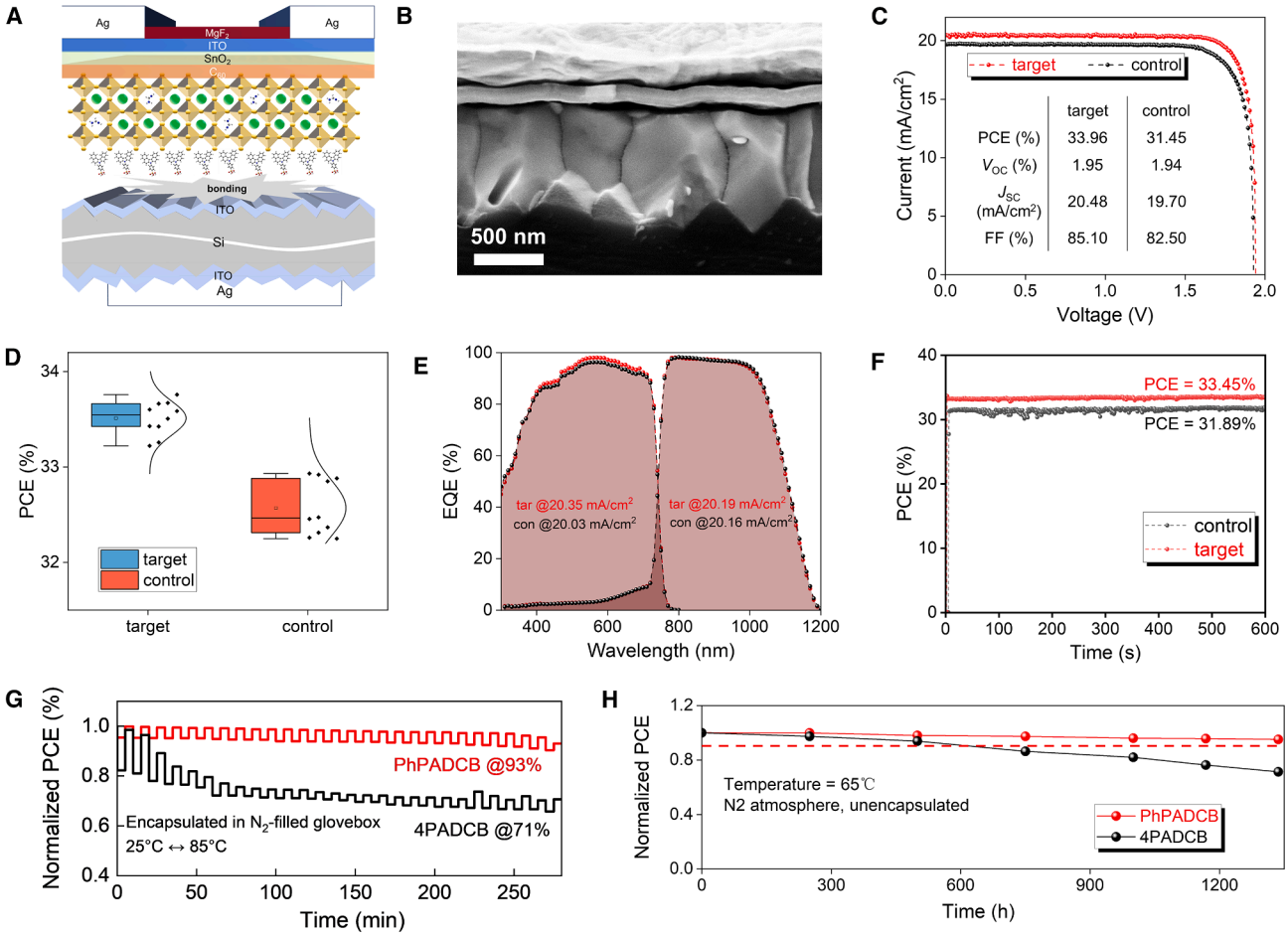

Figure 5. PhPADCB enables high-efficiency and thermally stable perovskite/silicon tandem solar cells

(A) Schematic illustration of the perovskite/silicon tandem structure; (B) cross-sectional SEM image of the perovskite spin-coated on silicon; (C) best *J-V* curve of the perovskite/silicon tandem device fabricated using PhPADCB and 4PADCB; (D) comparison of device statistical efficiencies between 4PADCB and PhPADCB; (E) EQE spectra of the perovskite/silicon tandem cells; (F) SPO of the tandem cell; (G) thermal cycling stability of encapsulated perovskite/silicon tandem solar cells; (H) thermal stability during storage in a glovebox at 65°C.

Furthermore, to verify the uniform coverage of PhPADCB on textured silicon substrates, we conducted EDS and secondary ion mass spectrometry (SIMS) measurements to evaluate its spatial uniformity. The EDS results are presented in Figures S43–S45. Silicon samples coated with PhPADCB and 4PADCB, respectively, were analyzed by performing elemental scans at five different locations. The results for the control and target samples are summarized in Figure S45. Compared with the control sample, the target sample exhibits a more uniform distribution and a higher proportion of the P element, which provides additional evidence supporting the superior coverage behavior of PhPADCB on textured silicon surfaces.

Additionally, we performed time of flight secondary ion mass spectrometry (TOF-SIMS) characterization on silicon substrates directly coated with SAMs (Figures S46 and S47). The target group exhibits a markedly higher oxygen signal than the control group, along with a more uniform spatial distribution. These observations are consistent with the EDS results discussed above, further confirming that PhPADCB forms a more homogeneous and densely packed SAM.

Similarly, for the perovskite films grown on silicon substrates modified with the two SAMs, the inherent thinness and fragility of the silicon substrate make it practically unfeasible to decouple the film for direct buried-interface stress characterization. Consequently, we utilized ultrathin perovskite films with partial coverage of the silicon pyramids to reflect the stress state at the buried interface, as shown in Figures S48 and S49. Perovskite precursor solutions with concentrations of 0.3 and 1.6 mM were spin-coated onto the SAM-modified silicon bottom cells, followed by thermal annealing at 120°C for 30 min.

Notably, the nanomechanical mapping of the ultrathin perovskite films (0.3 mM) reveals a distinct difference in the stress state between the pyramid tips and valleys. For the 4PADCB group, the average Young's modulus values before and after annealing were 2.801 and 3.043 GPa at 0.3 mM and 2.182 and 2.364 GPa at 1.6 mM, respectively, accompanied by evident localized stress concentration at these specific topological

features (Figure S48). In contrast, the PhPADCB group exhibited more stable modulus values of 2.390 GPa (before) and 2.429 GPa (after) at 0.3 mM and 2.186 GPa (before) and 2.309 GPa (after) at 1.6 mM. The more dispersed stress distribution observed across both the tips and the valleys in the PhPADCB group provides direct evidence for its capacity to mitigate thermal stress at the textured buried interface.

The strong anchoring and upright orientation of the SAM reduce defect formation and mitigate stress accumulation during thermal cycling, preserving uniform interfacial contact. This improved interface stability contributes independently to maintaining efficient charge extraction and overall device performance, beyond the effects of charge transport and band alignment. As illustrated in Figure 5G, the encapsulated perovskite/silicon tandem solar cells were subjected to thermal cycling between 25°C and 85°C within a nitrogen-filled glovebox. After 280 h of cycling, the PhPADCB-based device maintains 93% of its initial PCE, whereas that of the 4PADCB-based device drops significantly to 71%. Finally, both types of tandem devices were placed on a 65°C hotplate inside a nitrogen-filled glovebox for continuous thermal aging, during which their *J-V* characteristics were periodically measured. The resulting normalized PCE as a function of time is shown in Figure 5H. After 1,350 h of heating, the PhPADCB-based device retains more than 90% of its initial PCE, whereas that of the 4PADCB-based device degrades to about 70% of its original value, further confirming the superior thermal stability of PhPADCB.

Conclusions

In summary, we demonstrate that the application of structurally tailored SAMs enables conformal deposition and uniform monolayer coverage on textured substrates while simultaneously modulating perovskite ionic migration and crystallographic orientation and alleviating lattice strain at the buried interface. The rigid, conjugated PhPADCB molecule provides stronger interfacial anchoring, a more upright molecular orientation, and conformal monolayer uniformity, while its biphenyl head group efficiently passivates lattice defects at the perovskite bottom interface. Moreover, the strong binding of this SAM to both ITO and the perovskite (100) planes not only suppress ionic migration but also reduces the accumulation of thermal stress in tandem devices. As a result, PhPADCB-based wide-band-gap perovskite solar cells achieve a PCE of 23.77% (V_{OC} = 1.27 V, J_{SC} = 22.13 mA cm^{-2}, *FF* = 84.63%) and retain 91% of its initial efficiency after 1,500 h of continuous operation.

When applied to perovskite/silicon tandem devices, this strategy yields a PCE of 33.96% (reverse scan, V_{OC} = 1.95 V, J_{SC} = 20.48 mA cm^{-2}, *FF* = 85.10%), surpassing that of 4PADCB-based devices by 2.51 percentage points (with a certified efficiency of 33.72%). Meanwhile, the SPO of the tandem cell reached a stable 33.45% after 600 s. In addition to the obtained efficiency, the PhPADCB-based interface demonstrated enhanced stability under thermal stress. Encapsulated tandem devices retained 93% of their initial efficiency after 280 h of thermal cycling (25°C–85°C) and maintained over 90% of their initial PCE after 1,350 h of continuous thermal aging at 65°C, outperforming their 4PADCB-based counterparts. These findings highlight the role of molecular rigidity in constructing stable, well-oriented, and electronically coherent interfaces, offering a generalizable route toward further efficiency improvements in scalable tandem photovoltaics.

METHODS

Key experimental procedures, including material preparation, SAM deposition, perovskite film fabrication, single-junction and perovskite/silicon tandem device fabrication, photovoltaic characterization, structural and optoelectronic characterization, computational analysis, and stability testing, are described in detail in the supplemental methods. Further details regarding materials, device fabrication, characterization conditions, computational methods, and data analysis can be found in the supplemental information.

RESOURCE AVAILABILITY

Lead contact

Requests for further information and resources should be directed to and will be fulfilled by the lead contact, Guojia Fang (gjfang@whu.edu.cn).

Materials availability

PhPADCB and other materials used in this study are available from the lead contact upon reasonable request and subject to availability and institutional regulations.

Data and code availability

All data reported in this paper will be shared by the lead contact upon reasonable request. This paper does not report original code.

ACKNOWLEDGMENTS

This work was supported by the Key Research and Development Program of the Ministry of Science and Technology of China (grant no. 2024YFE0201800) and the National Natural Science Foundation of China (grant nos. 12134010, 12404095, 12174290, and 62304158). The authors gratefully acknowledge the Public Scientific Research Platform of Wuhan University for providing access to AFM, SEM, and EDS facilities and the School of Physics at Wuhan University for access to UPS, XPS, AFM, and XRD instrumentation. They also acknowledge the Public Scientific Research Platform and the Computing Center of Wuhan University for their support in material characterization. The authors thank Dr. Zhang Ying from the Core Facility of Wuhan University for her assistance with the TOF-SIMS analysis, and they also thank the Core Facility of Wuhan University for access to TOF-SIMS instrumentation.

AUTHOR CONTRIBUTIONS

S.D. conceived the study, designed the experiments, developed the methodology, performed most of the experimental work, fabricated and characterized the perovskite and perovskite/silicon tandem solar cells, analyzed and visualized the data, and wrote the original draft. M.H. contributed to selected experiments and characterization measurements. Z.Z. provided and characterized the silicon bottom cells and contributed to the related data analysis. J.L., F.Y., Y.G., and K.G. contributed to material and device characterization. T.G., X.X., and E.B. provided technical information, experimental conditions, and guidance related to the silicon bottom cells and perovskite/silicon tandem devices. W.K. and G.F. provided experimental resources and research support. G.F. supervised the project and revised the manuscript. All authors discussed the results and approved the final version of the manuscript.

DECLARATION OF INTERESTS

The authors declare no competing interests.

SUPPLEMENTAL INFORMATION

Supplemental information can be found online at https://doi.org/10.1016/j.joule.2026.102597.

Received: December 26, 2025
Revised: March 18, 2026
Accepted: July 7, 2026

REFERENCES

1. Jia, L., Xia, S., Li, J., Qin, Y., Pei, B., Ding, L., Yin, J., Du, T., Fang, Z., Yin, Y., et al. (2025). Efficient perovskite/silicon tandem with asymmetric self-assembly molecule. Nature *644*, 912–919. https://doi.org/10.1038/s41586-025-09333-z.
2. Wu, W., Gao, H., Jia, L., Li, Y., Zhang, D., Zhan, H., Xu, J., Li, B., Geng, Z., Cheng, Y., et al. (2025). Stable and uniform self-assembled organic diradical molecules for perovskite photovoltaics. Science *389*, 195–199. https://doi.org/10.1126/science.adv4551.
3. Yang, G., Deng, C., Li, C., Zhu, T., Liu, D., Bai, Y., Chen, Q., Huang, J., and Li, G. (2025). Towards efficient, scalable and stable perovskite/silicon tandem solar cells. Nat. Photon. *19*, 913–924. https://doi.org/10.1038/s41566-025-01732-y.
4. Er-Raji, O., Messmer, C., Pradhan, R.R., Fischer, O., Hnapovskyi, V., Kosar, S., Marengo, M., List, M., Faisst, J., Jurado, J.P., et al. (2025). Electron accumulation across the perovskite layer enhances tandem solar cells with textured silicon. Science *390*, eadx1745. https://doi.org/10.1126/science.adx1745.
5. Wang, W., Liang, H., Ding, Y., Wu, H., Zhou, W., Wen, X., Ma, M., Li, W., Liu, G., Ye, S., et al. (2025). Super-hydrophilic SAMs via chlorine-substituted all-hydrophilic molecule modification for monolithic perovskite-silicon tandem solar cells. Adv. Energy Mater. *15*, 2502222. https://doi.org/10.1002/aenm.202502222.
6. Fang, L., Ren, M., Li, B., Liu, X., Liang, S., Petermann, J., Gholipoor, M., Zhao, T., Sutter, J., Fassl, P., et al. (2025). Interfacial design strategies for stable and high-performance perovskite/silicon tandem solar cells on industrial silicon cells. Nat. Commun. *16*, 8881. https://doi.org/10.1038/s41467-025-64467-y.
7. Guo, C., Du, H.Q., Wang, Y.C., Gao, X., Lan, Y.Q., Xiao, Y.S., Jiang, W., Zhou, Y.C., Yuan, Q.B., Qiang, Z.Y., et al. (2025). Bifacially reinforced self-assembled monolayer interfaces for minimized recombination loss and enhanced stability in perovskite/silicon tandem solar cells. Adv. Mater. *37*, e2504520. https://doi.org/10.1002/adma.202504520.
8. Jiang, W., Qu, G., Huang, X., Chen, X., Chi, L., Wang, T., Wong, C.-T., Lin, F.R., Yang, C., Jiang, Q., et al. (2025). Toughened self-assembled monolayers for durable perovskite solar cells. Nature *646*, 95–101. https://doi.org/10.1038/s41586-025-09509-7.
9. Yang, J., Qu, G., Qiao, Y., Cai, S., Hu, J., Geng, S., Li, Y., Jin, Y., Shen, N., Chen, S., et al. (2025). Flexibility meets rigidity: a self-assembled monolayer materials strategy for perovskite solar cells. Nat. Commun. *16*, 6968. https://doi.org/10.1038/s41467-025-62388-4.
10. Huang, C., Yang, Y., Liu, C., Chen, H., Chaudhuri, S., Jeon, W.C., Li, M., Rolston, N., Bati, A.S.R., Gilley, I.W., et al. (2025). Electrostatically enhanced buried interface binding of self-assembled monolayers for efficient and stable inverted perovskite solar cells. Adv. Mater. *37*, e08740. https://doi.org/10.1002/adma.202508740.
11. Wu, J., Yan, P., Yang, D., Guan, H., Yang, S., Cao, X., Liao, X., Ding, P., Sun, H., and Ge, Z. (2024). Bisphosphonate-anchored self-assembled molecules with larger dipole moments for efficient inverted perovskite solar cells with excellent stability. Adv. Mater. *36*, e2401537. https://doi.org/10.1002/adma.202401537.
12. Chen, Q., Sun, K., Franco, L.R., Wu, J., Öhrström, L., Liu, X., Gumbo, M., Ozório, M.S., Araujo, C.M., Zhang, G., et al. (2025). Effects of alkyl spacer length in carbazole-based self-assembled monolayer materials on molecular conformation and organic solar cell performance. Adv. Sci. (Weinh) *12*, e2410277. https://doi.org/10.1002/advs.202410277.
13. Chen, C.H., Liu, G.W., Chen, X., Deger, C., Jin, R.J., Wang, K.L., Chen, J., Xia, Y., Huang, L., Yavuz, I., et al. (2025). Methylthio substituent in SAM constructing regulatory bridge with photovoltaic perovskites. Angew. Chem. Int. Ed. *64*, e202419375. https://doi.org/10.1002/anie.202419375.
14. Zhang, Z., Xu, Y., Chen, S., Li, W., Wang, S., Peng, C., Du, S., Li, S., Zhao, X., Wang, T., et al. (2025). Monodisperse regulation of self-assembled monolayer via dipole molecules for efficient perovskite solar cells. Angew. Chem. Int. Ed. *64*, e202512660. https://doi.org/10.1002/anie.202512660.
15. Luo, C., Zhou, Q., Wang, K., Wang, X., He, J., Gao, P., Zhan, C., Bi, Z., Li, W., Ma, Y., et al. (2025). Engineering bonding sites enables uniform and robust self-assembled monolayer for stable perovskite solar cells. Nat. Mater. *24*, 1265–1272. https://doi.org/10.1038/s41563-025-02275-x.
16. Wang, J., Jiao, B., Tian, R., Sun, K., Meng, Y., Bai, Y., Lu, X., Han, B., Yang, M., Wang, Y., et al. (2025). Less-acidic boric acid-functionalized self-assembled monolayer for mitigating NiOx corrosion for efficient all-perovskite tandem solar cells. Nat. Commun. *16*, 4148. https://doi.org/10.1038/s41467-025-59515-6.
17. Feng, Y., Wang, Y., Yang, H., Li, S., Luo, J., Han, X., Alshahrani, T., Mai, B., Wang, D., Ding, Z., et al. (2025). Homogenized self-assembled molecules for inverted perovskite solar cells. Angew. Chem. Int. Ed. *64*, e202505876. https://doi.org/10.1002/anie.202505876.
18. Zhang, X., Wang, Y., Zhang, K., Tao, M., Guo, H., Guo, L., Song, Z., Wen, J., Yang, Y., Hou, Y., et al. (2025). Reinforcing coverage of self-assembled monomolecular layers for inverted perovskite solar cells with efficiency of 25.70%. Angew. Chem. Int. Ed. *64*, e202423827. https://doi.org/10.1002/anie.202423827.
19. Ji, Y., Liang, L., Chen, T., Liu, X., Mao, M., Hu, Y., Jin, Y., Huang, X., Ren, X., Xie, D., et al. (2025). High-performance ultrathin flexible organic solar cells through the modification of self-assembled monolayers. Adv. Energy Mater. *15*, 2501698. https://doi.org/10.1002/aenm.202501698.
20. Ying, Z., Su, S., Li, X., Chen, G., Lian, C., Lu, D., Zhang, M., Guo, X., Tian, H., Sun, Y., et al. (2025). Antisolvent seeding of self-assembled monolayers for flexible monolithic perovskite/Cu(In,Ga)Se2 tandem solar cells. Nat. Energy *10*, 737–749. https://doi.org/10.1038/s41560-025-01760-6.
21. Qu, G., Zhang, L., Qiao, Y., Gong, S., Ding, Y., Tao, Y., Cai, S., Chang, X.-Y., Chen, Q., Xie, P., et al. (2025). Self-assembled materials with an ordered hydrophilic bilayer for high performance inverted perovskite solar cells. Nat. Commun. *16*, 86. https://doi.org/10.1038/s41467-024-55523-0.
22. Lepikko, S., Jaques, Y.M., Junaid, M., Backholm, M., Lahtinen, J., Julin, J., Jokinen, V., Sajavaara, T., Sammalkorpi, M., Foster, A.S., et al. (2023). Droplet slipperiness despite surface heterogeneity at molecular scale. Nat. Chem. *16*, 506–513. https://doi.org/10.1038/s41557-023-01346-3.
23. Aydin, E., Ugur, E., Yildirim, B.K., Allen, T.G., Dally, P., Razzaq, A., Cao, F., Xu, L., Vishal, B., Yazmaciyan, A., et al. (2023). Enhanced optoelectronic coupling for perovskite/silicon tandem solar cells. Nature *623*, 732–738. https://doi.org/10.1038/s41586-023-06667-4.
24. Xie, Y., Tian, J., Yang, X., Chen, J., Yu, S., Tang, D., Hu, X., Sun, Y., and Lv, M. (2025). Thiophene expanded self-assembled monolayer as hole transport layer for organic solar cells with efficiency of 20.78%. Adv. Mater. *37*, e02485. https://doi.org/10.1002/adma.202502485.
25. Zhu, C., Chen, T., Guan, S., Li, S., Zhang, Y., Wang, M., Yao, N., Wupur, A., Shi, M., Li, H., et al. (2025). A spiro-configured self-assembled molecule as hole transport material for organic solar cells featuring high-efficiency and universality. Adv. Energy Mater. *15*, 2504541. https://doi.org/10.1002/aenm.202504541.

26. Wu, Y., Dolgormaa, A., Zhang, Y., Yang, L., Yao, B., Zhan, H., Cheng, Y., Wang, L., and Qin, C. (2025). Improving buried interface contact by diphenylphosphine oxide substituent for highly efficient inverted perovskite solar cells. Nano Energy *143*, 111319. https://doi.org/10.1016/j.nanoen.2025.111319.

27. Wei, Z., Zhou, Q., Niu, X., Liu, S., Dong, Z., Liang, H., Chen, J., Shi, Z., Wang, X., Jia, Z., et al. (2025). Surpassing 90% Shockley–Queisser V_{OC} limit in 1.79 eV wide-bandgap perovskite solar cells using bromine-substituted self-assembled monolayers. Energy Environ. Sci. *18*, 1847–1855. https://doi.org/10.1039/d4ee04029e.

28. Hu, S., Zeng, S., Deng, X., Hou, P., Du, H., Dou, Y., Xiong, W., Pan, J., Peng, Y., Cheng, Y.-B., et al. (2025). Scalable impregnation method for preparing a self-assembled monolayer in high-performance vapor-deposited lead-halide perovskite solar cells. ACS Nano *19*, 15018–15029. https://doi.org/10.1021/acsnano.5c01479.

29. Kim, S.Y., Kim, C.Y., Park, J.H., Woo, M.Y., Kim, D.H., Oh, O.J., Jeong, M.J., Jeon, S.W., Ahn, J.W., Shin, C.H., et al. (2025). Harmonious layer design in wide-bandgap p-i-n perovskite solar cells using carbazole and triazatruxene-based molecules. Small *21*, e2505638. https://doi.org/10.1002/smll.202505638.

30. Luo, Y., Tian, Y., Zhao, K., Mao, W., Liu, C., Shen, J., Cheng, Z., Değer, C., Miao, X., Zhang, Z., et al. (2025). Inductive effects in molecular contacts enable wide-bandgap perovskite cells for efficient perovskite/TOPCon tandems. Nat. Commun. *16*, 4516. https://doi.org/10.1038/s41467-025-59896-8.

31. Gao, D., Li, B., Sun, X., Liu, Q., Zhang, C., Qian, L., Yu, Z., Li, X., Wu, X., Liu, B., et al. (2025). High-efficiency perovskite solar cells enabled by suppressing intermolecular aggregation in hole-selective contacts. Nat. Photon. *19*, 1070–1077. https://doi.org/10.1038/s41566-025-01725-x.

32. Zhou, B., Li, M., Xiong, Q., Zhang, L., Zhang, S., Sun, J., Tang, J., and Choy, W.C.H. (2025). Soft conjugation extension strategy of self-assembled molecules for achieving efficient and mechanically stable flexible perovskite solar cells. Energy Environ. Sci. *18*, 8803–8814. https://doi.org/10.1039/d5ee03823e.

33. Yin, X., Zhao, Y., Pei, C., Wang, Z., Sun, Y., Zhang, M., Hao, Y., Wei, X., Zhao, Z., Dong, K., et al. (2025). Stress release of single crystal arrays bridged by SAM interface toward highly mechanically durable flexible perovskite NIR photodetector. Adv. Mater. *37*, e2413721. https://doi.org/10.1002/adma.202413721.

34. Wang, L., Wang, N., Wu, X., Liu, B., Liu, Q., Li, B., Zhang, D., Kalasariya, N., Zhang, Y., Yan, X., et al. (2025). Highly efficient monolithic perovskite/TOPCon silicon tandem solar cells enabled by "halide locking". Adv. Mater. *37*, e2416150. https://doi.org/10.1002/adma.202416150.

35. Caprioglio, P., Smith, J.A., Oliver, R.D.J., Dasgupta, A., Choudhary, S., Farrar, M.D., Ramadan, A.J., Lin, Y.-H., Christoforo, M.G., Ball, J.M., et al. (2023). Open-circuit and short-circuit loss management in wide-gap perovskite p-i-n solar cells. Nat. Commun. *14*, 932. https://doi.org/10.1038/s41467-023-36141-8.

36. Li, R., Zhang, D., Wei, J., Li, B., Xin, H., Hang, P., Ni, Z., Yang, D., and Yu, X. (2025). n-type regulation of 2D perovskite interlayers for efficient perovskite-silicon tandem solar cells. Joule *9*, 102141. https://doi.org/10.1016/j.joule.2025.102141.

37. Li, C., Chen, Y., Li, Y., Zhang, Z., Yang, J., Wang, Y., Gong, L., Yuan, Z., Liang, L., Liu, S., et al. (2025). Achieving 32% efficiency in perovskite/silicon tandem solar cells with bidentate-anchored superwetting self-assembled molecular layers. Angew. Chem. Int. Ed. *64*, e202502730. https://doi.org/10.1002/anie.202502730.

38. Shi, C., Wang, J., Lei, X., Zhou, Q., Wang, W., Yang, Z., Liu, S., Zhang, J., Zhu, H., Chen, R., et al. (2025). Modulating competitive adsorption of hybrid self-assembled molecules for efficient wide-bandgap perovskite solar cells and tandems. Nat. Commun. *16*, 3029. https://doi.org/10.1038/s41467-025-58111-y.

39. Li, Y., Qiao, Y., Yang, J., Shen, N., Shen, H., Jin, Y., Qu, G., Li, S., Sheng, Y., Yao, J., et al. (2025). Modulating adsorption configurations of hybrid self-assembled molecules enables high-performance inverted perovskite solar cells. Adv. Mater. *38*, e14623. https://doi.org/10.1002/adma.202514623.

40. Kim, J., Park, J., Lim, J., Kim, J., Kim, J., Shin, N., Yun, J.S., Im, J., and Il Seok, S. (2025). Susceptible organic cations enable stable and efficient perovskite solar cells. Joule *9*, 101879. https://doi.org/10.1016/j.joule.2025.101879.

41. Zheng, J., Wang, G., Duan, L., Duan, W., Jiang, Y., Pearce, P., Gao, Y., Mahmud, M.A., Liao, C., Leung, T.L., et al. (2025). Tailoring nanoscale interfaces for perovskite–perovskite–silicon triple-junction solar cells. Nat. Nanotechnol. *20*, 1648–1655. https://doi.org/10.1038/s41565-025-02015-x.

42. Gao, M., Ou, Z., Wang, C., Liu, L., Hu, D., Wan, W., Chen, P., Pan, Y., Nie, S., Luo, Y., et al. (2025). Multifunctional buried molecule-bridge for high-performance inverted perovskite solar cells. Adv. Mater. *38*, e14273. https://doi.org/10.1002/adma.202514273.